Characterization of Mutli-Material Interfaces in PolyJet Additive Manufacturing

Ivan Vu[*], Lindsey Bass[†], Nicholas Meisel[†], Bruce Orler[§],
Christopher B. Williams[†], David A. Dillard[*]

[*] Biomedical Engineering and Mechanics Department
[†] Mechanical Engineering Department
[§] Chemistry Department
Macromolecules and Interfaces Institute
Virginia Tech, Blacksburg, VA 24061

REVIEWED

Abstract

Relatively few engineering devices and structures are monolithic, as combinations of materials are often needed to obtain the necessary functionality, performance, weight, and cost requirements. Progress in additive manufacturing now allows multiple materials and even blends of materials to be produced in a single manufacturing process, opening new opportunities for expeditiously achieving functional and performance targets. Just as interactions at interfaces have long been of interest in the area of adhesive bonding, similar issues need to be addressed for printed composite materials. In this study, a Stratasys PolyJet system was used to produce configurations consisting of a soft acrylic layers (TangoBlackPlus) sandwiched by two stiffer acrylic strips (VeroWhitePlus). Several test methods based on the double cantilever beam specimen, a common experimental approach to characterize adhesive performance, were evaluated to characterize the fracture resistance of the assembled layers. Failures nominally occurred at the interface between the two types of materials. Further testing is providing insights into the effects of print direction, postcuring, and interface architecture on the resulting fracture energies. These studies suggest the opportunities for designing printed interfaces with improved performance and durability for multi-material additive manufacturing products.

1. INTRODUCTION

Additive manufacturing (AM) is a unique alternative to traditional manufacturing techniques that embraces the concept of reducing product development cycles and shortening the time-to-market of new products [1]. AM has become a popular method to produce not only prototypes and molds, but increasingly AM is being used to fabricate components for engineered products for a range of industrial applications. AM production of multi-material components and devices is of considerable interest, as it allows the fabrication of elastomeric hinges, integrated grips, and other products where material changes can achieve enhanced functionality [2], reduced part counts, and streamlined assembly. The ability to selectively place multiple materials with different mechanical properties offers design freedom for producing final parts with tunable failure locus and resistance to fracture.

Even with rapid advances of AM technologies, there are still a number of concerns that need to be addressed. For fabrication with a single material, porosity and anisotropy can be issues due to associated with the layer-by-layer printing process, the curing or solidification process, and other factors. Imperfect or weak bonding between layers can lead to delamination and breakage under stress [3, 4]. Surface finishes are often poor and can introduce porosity, making prototypes susceptible to moisture infiltration [4]. Previous research has confirmed print build orientation has a significant effect on the mechanical properties in uniaxial tension of a number of AM systems [5-8], including those printed with multiple polymers. Researchers have primarily employed the common dog-bone tensile test specimen in their studies of modulus, strength, and fatigue resistance [5, 7, 9-12]. However, to our knowledge, no literature has addressed the characterization of fracture resistance of these materials for mode I fracture (opening mode; wherein tensile stress occurs normal to the plane of the crack).

Recognizing prior studies of strength of monolithic and multi-material systems, this study extends characterization by assessing the fracture behavior and resistance of additively manufactured materials tested in laminated beam specimens. Specifically, trilayer constructions involving two printed polymers are used, which results in specimens resembling adhesively bonded joints. Several specimen geometries are developed and evaluated, including double cantilever beam (DCB), tapered double cantilever beam (TDCB), and peel configurations, all of which have origins in commonly used fracture tests for adhesive bonded joints and laminated composites. The fracture energy and locus of failure are important characteristics used to evaluate the performance of adhesive bonds, and we believe these properties are also important for AM materials, including those containing interfaces between dissimilar components. Of specific interest is whether these interfaces are inherently weaker than the surrounding bulk materials, resulting in a weakened region that could lead to product failure under quasi-static, sustained, or cycling loading. This study focuses on measuring the quasi-static behavior or such interfaces, proposing specimens that may be appropriate for characterization of a range of AM systems. Properties obtained could be used to optimize multi-material compatibility and improve printing algorithms, perhaps through alternate patterning or architectures of interface, to result in stronger, tougher, and more durable products. The experimental methods employed in this study are presented in Section 2. Results are presented along with a discussion in Section 3. Closure is offered in Section 4.

2. EXPERIMENTAL METHODS

2.1. Materials

The materials involved in this study are two photopolymers used in the Stratasys PolyJet material jetting AM process (Stratasys, Eden Prairie, MN). In this process, layers of multiple acrylic-based photopolymers are selectively deposited onto a build tray via inkjet printing. The jetted photopolymers are quickly cured by UV lamps that are mounted on the printing block. Models printed by this process are incased in a sacrificial support material to ensure dimensional stability, though it can be easily removed after printing via water jet cleaning.

The material system of interest is the interface between two photopolymers: TangoBlackPlus (TB) and VeroWhitePlus (VW). TB is a black photopolymer that exhibits some rubber-like or elastomeric characteristics, while VW is a white, opaque photopolymer that is significantly stiffer in comparison to the TB. Their respective moduli, tensile strengths, and

glass transition temperatures (T_g) are conveyed in Table 1. Several researchers have studied this system in the past. Barclift et al. demonstrated when multiple VW parts are printed on the same tray, the part spacing has a significant effect on the mechanical properties [8]. Moore et al. analyzed fatigue strength of the TB/VW interface, indicating that the TB/VW interface failed prematurely in 25% of the dogbone specimens tested [2]. Sugavaneswaran et al. observed improved strength in a pure TB tensile specimen by implementing cylindrical reinforcements of VW throughout its structure [13].

Property	TangoBlackPlus (TB)	VeroWhitePlus (VW)
Young's Modulus (MPa)	0.1-0.3	2000-3000
Tensile Strength (MPa)	1.8-2.4	55-65
T_g (°C)	-10	52-54

Table 1. Table of material properties for TangoBlackPlus and VeroWhitePlus. Young's Modulus and T_g for TangoBlackPlus were not provided by manufacturer [14, 15].

2.2. Test Specimen Configurations and Fabrication

To evaluate the fracture resistance of trilayer specimens produced with this material system, several double cantilever beam [16, 17] and T-peel test [18] configurations, consisting of a TB layer sandwiched between VW layers, were designed, printed, and tested, In keeping with relevant literature and specimens for testing adhesive bonds, the VW layers will be referred to as adherends and the TB interlayer will be referred to as the adhesive, though these were in fact all printed in a single AM process via a Stratasys Connex 350 system. Each layer deposited is approximately 0.032 mm thick and for all specimens considered, the total thickness of the TB central layers is kept constant at 0.32 mm. The sandwich configuration and TB interlayer thickness were common to all specimens but were distinguished by the VW adherend thicknesses or method used to reinforce the adherend through bonded auxiliary adherends. These configurations, all of 9.9 mm width, included the following, each of which is illustrated in Figure 1:

- Aluminum-supported DCB (Al-DCB): 1 mm VW – 0.32 mm TB – 1 mm VW sandwiches bonded to 3.8 mm thick auxiliary aluminum adherends machined with endblocks.
- Fully-printed DCB (FP-DCB): 4.95 mm VW – 0.32 mm TB – 4.95 mm VW sandwiches with integral endblocks printed during fabrication.
- Steel-backed DCB (St-DCB): same as the unsupported DCB configuration but VW adherends are backed with 0.759 mm thick steel strips to reduce adherend deformation.
- TDCB: entire specimen, with 0.32 mm TB interlayer and varying adherend thickness printed in their entirety.
- T-peel: 0.32 mm VW – 0.32 mm TB – 0.32 mm VW sandwiches tested directly in T-peel configuration.
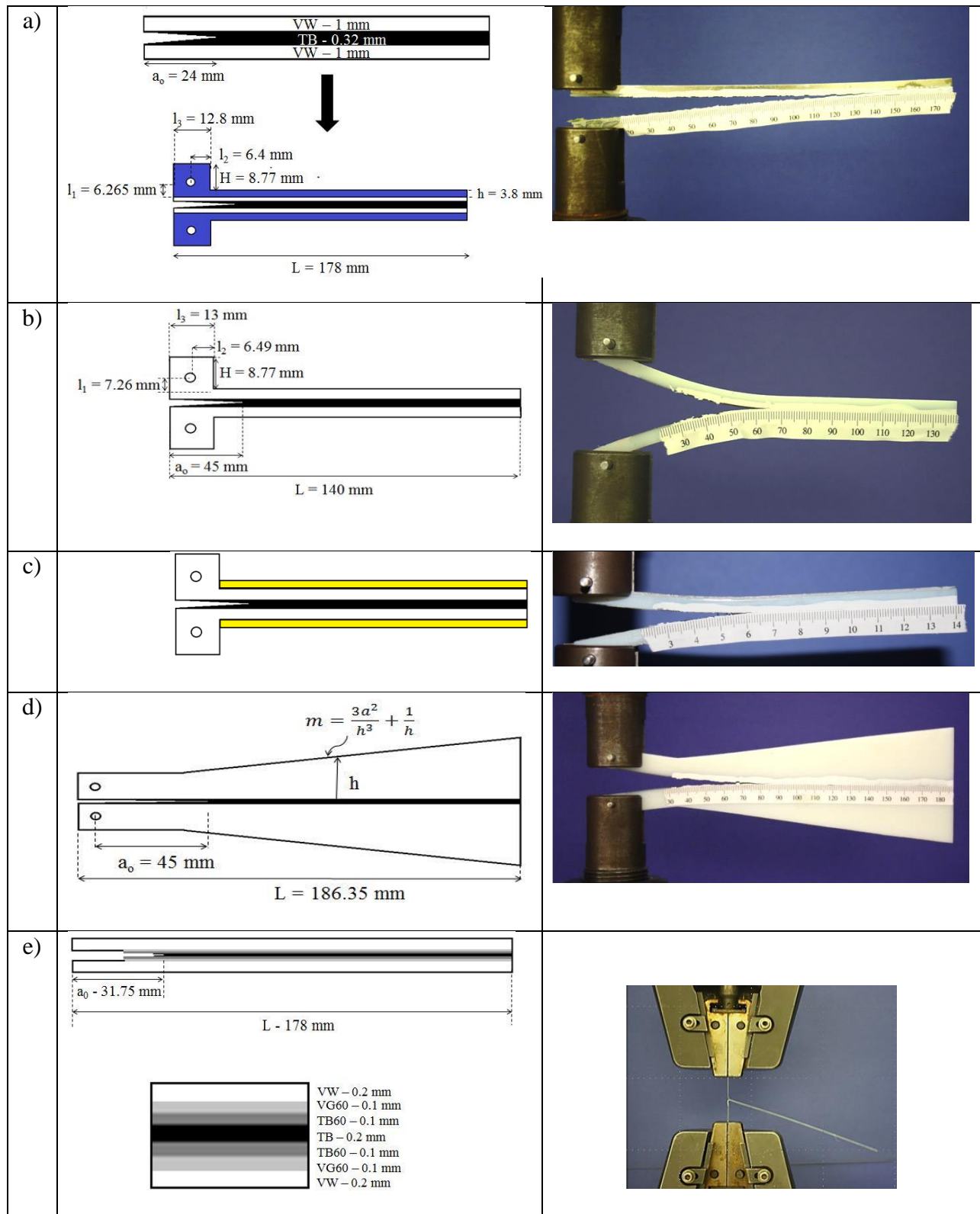
Figure 1. Illustrations of test configurations and photos of representative specimens during testing. Top to bottom are a) the aluminum-supported (AL-DCB), b) fully-printed (FP-DCB), and c) steel-backed DCB (St-DCB), d) TDCB, and e) T-peel geometries.

Expected to minimize printing costs and adherend dissipation, the aluminum-supported specimens were made by bonding printed sandwich strips between machined aluminum adherends. The sandwich strips contained a printed chevron notch in the TB interlayer to facilitate failure initiation within the interlayer. Prior to bonding, the 6061-T6 aluminum adherends were abraded with 120 grit sandpaper using a random orbital sander and cleaned in tap water using an ultrasonic cleaner (Fisher Scientific, Waltham, MA) for 3 minutes. The auxiliary adherends were dried in an oven at 110°C for 1 hour. The printed strips were bonded onto auxiliary aluminum adherends using commercially available LORD 320/322 epoxy adhesive (LORD Corporation. Cary, NC). A paper spacer was placed in the notch to prevent adhesive from bonding the initial crack. The specimens were clamped and left to cure at room temperature for 24 hours. After 4 hours of curing, excess adhesive was removed with a putty knife to allow visibility of the central layers for crack length measurements.

Though using more polymer, the fully-printed DCB specimens minimized ancillary specimen preparation, as they were ready to test without additional bonding procedures following printing. As shown in Figure 1, these specimens exhibited the most deformation during testing. Concerns with viscoelastic and plastic dissipation within the polymeric adherends led to the addition of 22 gauge (0.759 mm) steel strips, bonded to the back of the specimen arms using the bonding method described above. The steel-backed DCB resulted in somewhat smaller adherend deformations. Fully-printed TDCB specimens were also fabricated using the tapered profile generated according to the geometry factor m given by [16, 19]

$$m = \frac{3a^2}{h^3} + \frac{1}{h} \qquad\qquad 1$$

While typical adhesive have used a value of 2 for m when designing the TDCB [20, 21], a value of 3.5 is chosen for m in an effort to conserve material, while reducing the effects of dissipation and yielding of the adherends during testing. Though using the most printed polymer, these TDCB specimens resulted in reduced adherend deformation and are often advocated for adhesive testing because of the constant strain energy release rate nature of the specimen.

In addition to the four DCB configurations, T-peel tests were conducted to evaluate the peel resistance of the TB/VW interface. The same type of sandwich strips used for the aluminum supported DCB specimens were used in unsupported fashion as T-peel specimens. Variations of this configuration involving checkered patterns and interlayer gradient were also tested. The gradient version is illustrated in Figure 1; in addition to VB adherends and a TB central layer, blended layers of TangoBlackShore60 (TB60) and VeroGrey60 (VG60) were also incorporated.

2.3. Build Orientations

AM processes allow for components to be printed in different orientations, offering enhanced design and construction flexibility, but also resulting in nominally identical products with very different properties. In PolyJet, printed primitives are jetted in the direction of the travel of the printing block (X-axis); jetted 'lines' (composed of several individual drops) are rastered along the Y-axis to complete a layer. Subsequent layers are then built up in the Z-direction. The print resolution varies, with respective resolutions in the x-, y-, and z-directions of 0.043 mm, 0.043 mm (as per manufacturer-stated 600 dpi resolution), and 0.032 mm (when

printing multiple materials). Depending on the direction on any given fabricated item, adjacent material may effectively be co-cured, because of near simultaneous deposition, or can result when liquid monomer is deposited later on a cured layer. Of particular interest in this work is the effect orientation of the interfaces and interlayer resulting from the build direction has on the structural integrity of the fabricated product.
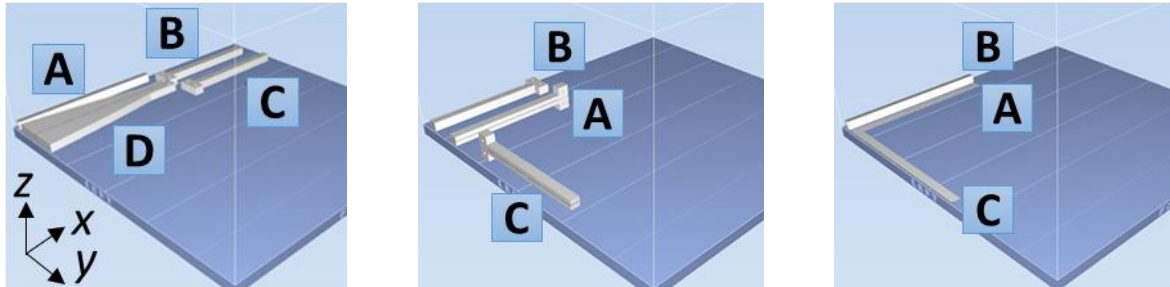
Figure 2. Illustration of various print orientations used to fabricate specimens. *Left*: xzy orientation for A) 3D printed (3DP) sandwich strips, B) and C) FP-DCB, and D) TDCB specimens. *Middle*: fully-printed DCB specimens oriented A) xyz, B) xzy, and C) yxz. *Right*: Al-DCB specimens oriented A) xyz, B) xzy, C) yxz.

For purposes here, a modified form of the orientation nomenclature given by ASTM52921-13 with reference to the TB interlayer [22] is used. The print orientation for each specimen will be designated by the plane of the interlayer and the direction of load application. For example, the DCB and TDCB specimens shown in the left portion of are printed in the $\bar{x}zy$ orientation, where the first letter ($\bar{x}$) indicates the direction of crack propagation; the second letter (z) is the direction of the specimen and interlayer width; and the last letter (y) is the direction of load application. Both FP-DCB specimens and the 3-D printed (3DP) strips used for Al-DCB specimens were printed in the $\bar{x}yz$, $\bar{x}zy$, and $\bar{y}xz$ -orientations to explore the effect of print orientation on fracture resistance, as shown in the middle and right images of Figure 2. AM strips, used for T-peel tests, were printed in the $\bar{x}yz$ orientation, as shown in the right portion of Figure 2.

2.4. Test Procedures

Typewriter correction fluid was applied to the TB bondline as an aid in visualizing the crack tip and paper rulers were affixed onto all DCB specimens in order to facilitate measurements of the crack length. Mode I tests were conducted using a 5800R Instron (Canton, MA) at a crosshead displacement rate of 1 mm/min, unless otherwise noted. Mode I fracture energies are calculated using corrected beam theory (CBT) [16, 19].

$$G_{\text{Ic}} = \frac{3P\delta}{2B(a+\hat{a})} \cdot \frac{F}{N} \qquad \qquad 2$$

where G_{Ic} is the applied mode I strain energy release rate; a is the crack length; P and δ are the applied load and the end displacement respectively at fracture propagation; F is the large displacement correction; N is the load block correction; B is the width of the specimen; and $\hat{a}$ is

the crack length correction. The large displacement correction F and the load block correction N are calculated by:

$$F = 1 - \frac{3}{10}\left(\frac{\delta}{a}\right)^2 - \frac{3}{2}\left(\frac{\delta l_1}{a^2}\right) \qquad 3$$

$$N = 1 - \left(\frac{l_2}{a}\right)^3 - \frac{9}{8}\left[1-\left(\frac{l_2}{a}\right)^2\right]\frac{\delta l_1}{a^2} - \frac{9}{35}\left(\frac{\delta}{a}\right)^2 \qquad 4$$

The crack correction $\hat{a}$ is used as a means to correct the crack length for a beam that is not perfectly built in. This correction is calculated by plotting the cube root of the compliance $(C/N)^{1/3}$ vs. the observed crack length a. Representative results are plotted in Figure 3. Extrapolation of the linear fit of this plot will yield $\hat{a}$ as the negative of the abscissa intercept. The R^2 value describes the accuracy of the linear fit in correlation to experimental data and given a value of 0.99, this provides further evidence that the CBT is works well for the calculation of fracture energy.

y = 0.0054x + 0.1253
R² = 0.9979
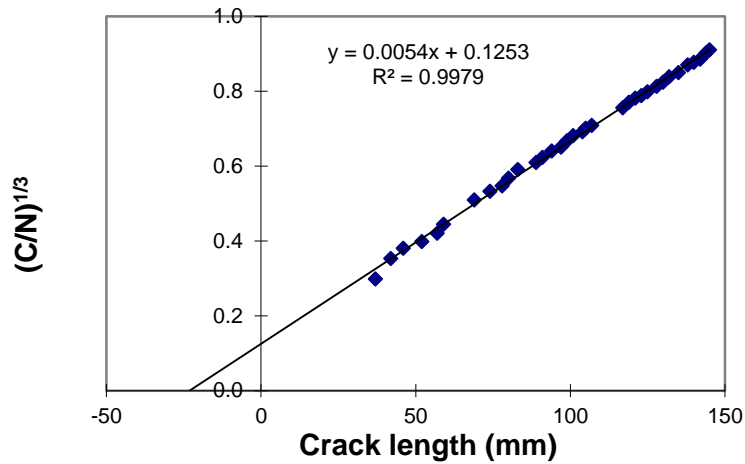
Figure 3. (C/N)1/3 vs. crack length a for aluminum DCB at 1 mm/min

As with the DCB, the mode I fracture energies for the TDCB are also calculated using CBT [16].

$$\mathcal{G}_{Ic} = \frac{4P^2}{E_s B^2} \cdot m \cdot \left[1 + 0.43\left(\frac{3}{m}\right)^{\frac{1}{3}} \cdot a^{\frac{-1}{3}}\right] \qquad 5$$

where E_s is Young's Modulus of VW and m is the specimen geometry factor previously described in Section 2.1.

The T-peel tests were performed at a crosshead displacement rate of 254 mm/min, in accordance to ASTM D1876 in the same Instron load frame. All of the above tests were conducted at room temperature.

3. RESULTS AND DISCUSSION

3.1. Specimen Comparison

To evaluate the proposed specimen configurations, samples were printed in the same orientation ($\bar{x}zy$-orientation) and interlayer thickness to assess the effectiveness of each configuration (Al-DCB, FP-DCB, St-DCB, TDCB; Section 2.2 and Figure 2). Tests were conducted within 1-2 days of printing in order to minimize effects of physical aging or other phenomena.
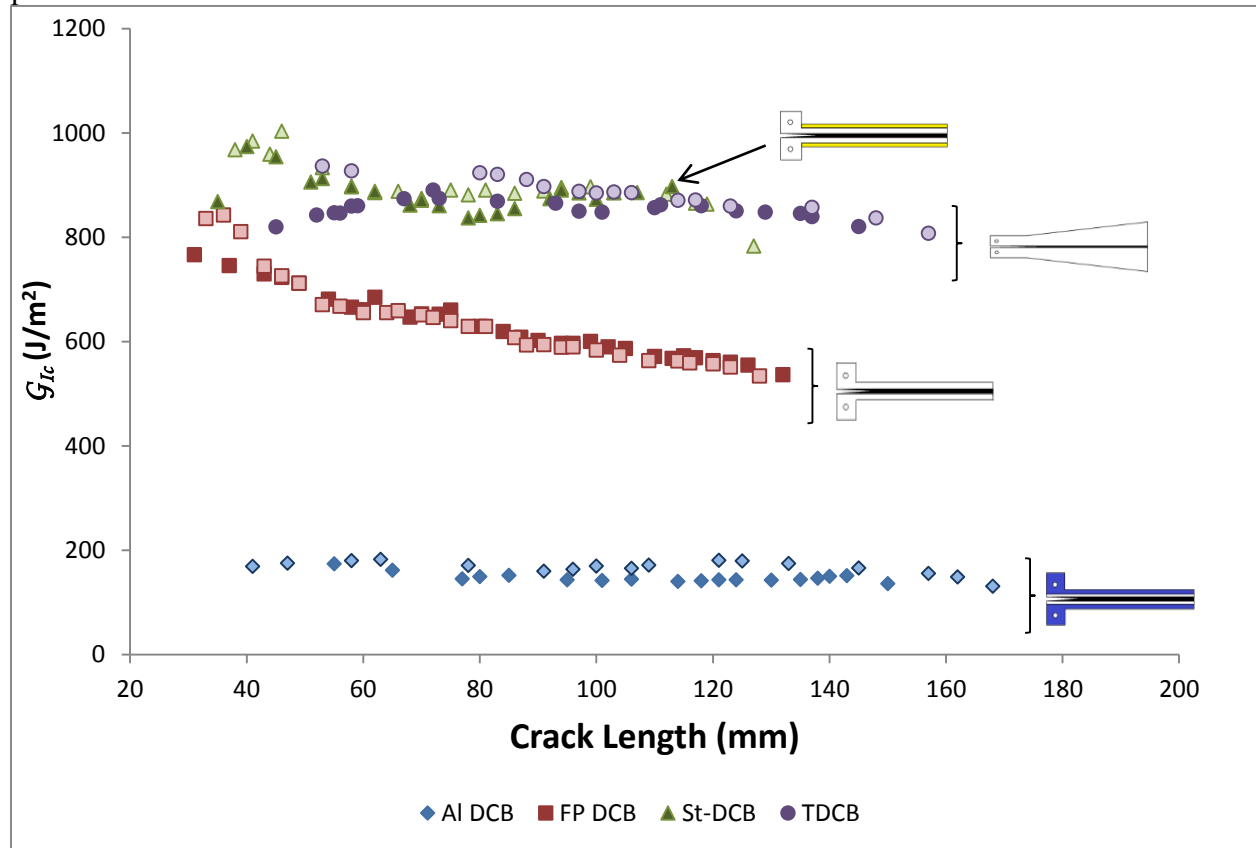
Figure **4** shows the variation of mode I fracture energy for all specimens, where two tests were conducted for each specimen type, with good consistency of the replicates.
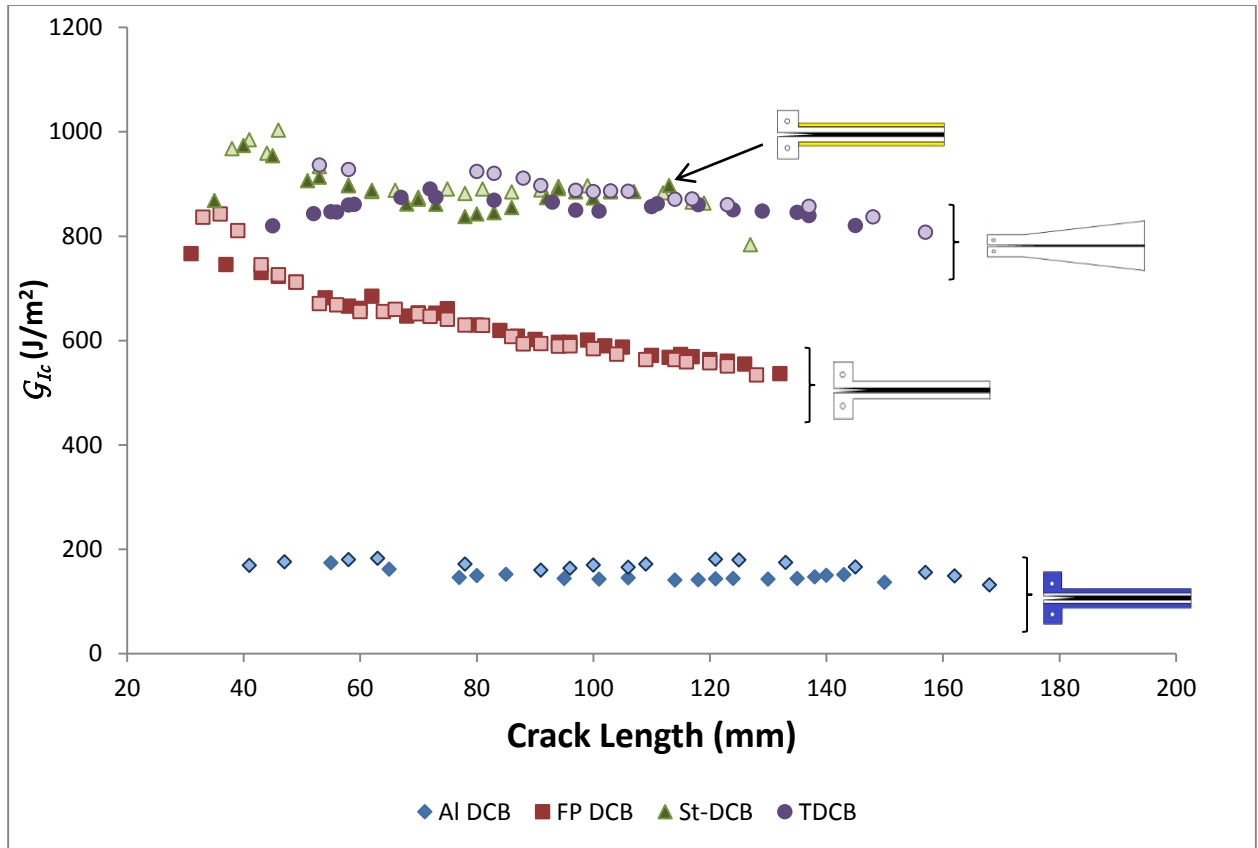
Figure 4. $\mathcal{G}_{Ic}$ vs. crack length for all DCB configurations in the $\vec{x}zy$-orientation: blue diamonds (AL-DCB), red squares (FP-DCB), green triangles (St-DCB), and purple circles (TDCB).

While data from two tests per specimen type are not statically significant, the results indicate that the analysis method demonstrates adequate repeatability. Optical photographs and SEM images of the fracture surfaces are shown in Figure 5. The Al-DCB configuration results in the lowest $\mathcal{G}_{Ic}$ of 148 ± 8 J/m^2 and the loci of failure is largely interfacial, though the failure meanders back and forth between the interfaces at a spatial scale of several millimeters. The layer boundaries are clearly seen in the Al-DCB configuration in Figure 5a, but overall the fracture surface is slightly smoother in comparison to the fully printed configurations.
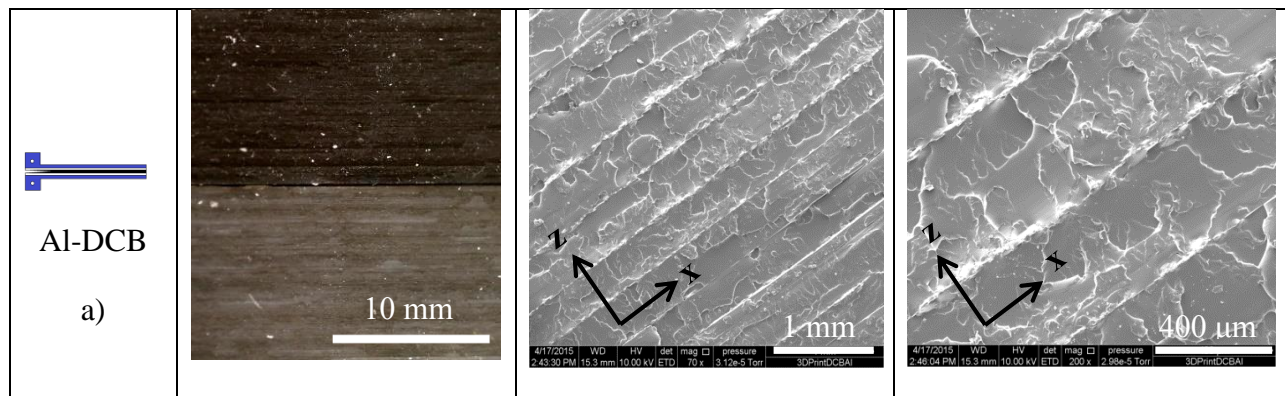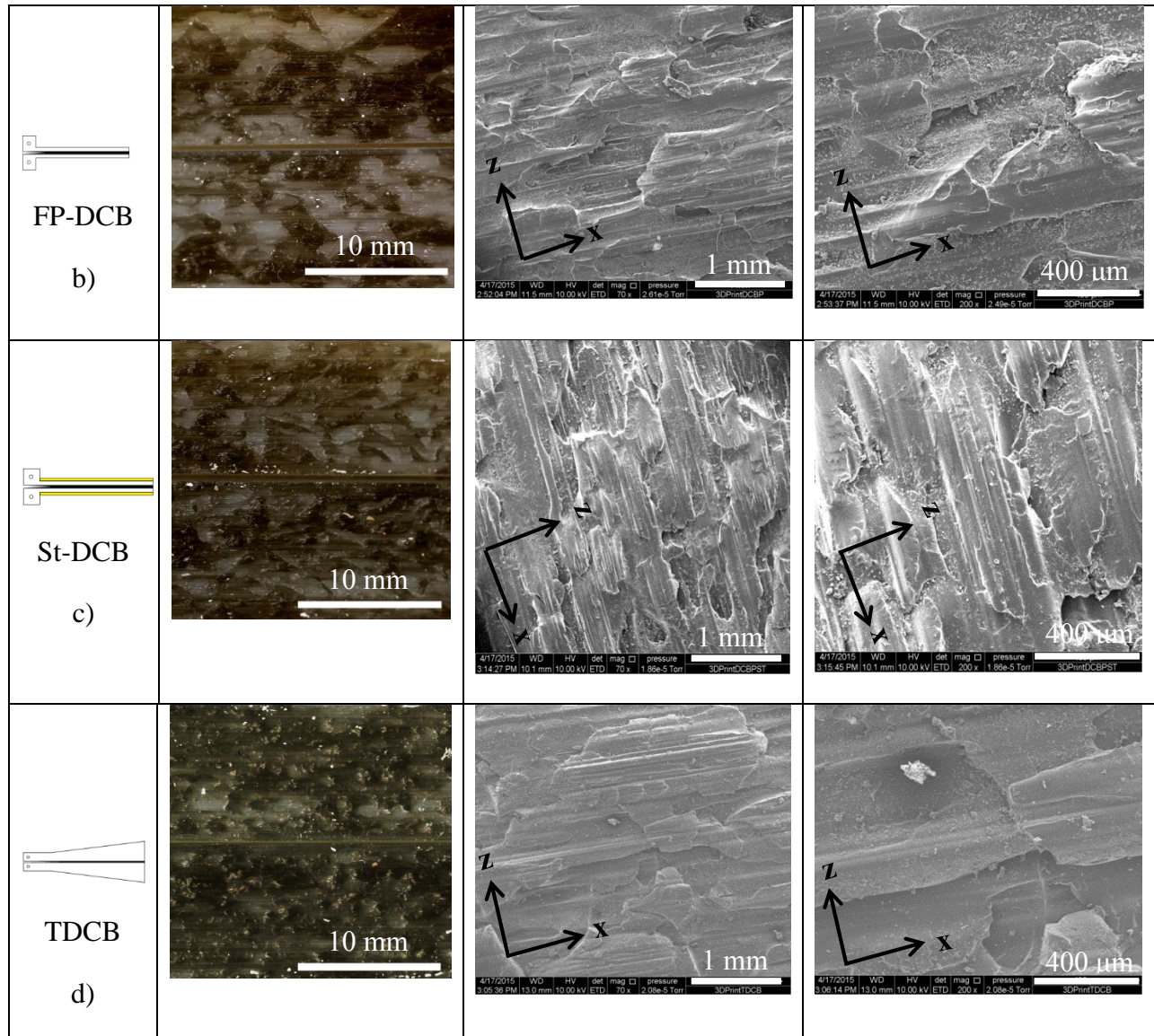
Figure 5. Failure surface of specimens with corresponding SEM images. Plane of the interlayer is oriented on the xz plane, with the direction of crack propagation aligned along the x axis

In contrast to the rather black and white failure surfaces that will be shown later for specimens prepared with other print orientations, the failure surfaces often appear grey to the naked eye. Polymer blending of the TB and VW may be occurring, as both VW and TB are deposited on each pass of the printer head, resulting in a potential interphase region that is much tougher than the less blended interface between the TB and VW. In the case of the Al-DCB, it is possible that the benefits of polymer blending, suspected for this print orientation with larger adherend thicknesses, were not achieved given the small dimensional scale of the printed assembly. Although surrounded by a thin layer of support material, it is plausible that as the roller repeatedly runs across the print path to level the deposited layers on such a narrow specimen, deformations, such as vibrations or smearing, compromised the structural integrity of the thin specimen. Some blending of the VW with the support material may have occurred as the

roller flattens the deposited droplets and reduced the properties, though it is not clear how this could have affected what appears to be a near interfacial failure to the interlayer. Increasing the thickness of the surrounding VW material could reduce the likelihood of polymer blending from occurring between the two materials or other anomalous effects that led to the very low fracture resistance of the Al-DCB specimens printed in this orientation. We do feel the very low properties likely arose from printing anomalies rather than the specimen configuration, *per se*.

The fully printed specimens were shown to develop polymer fibrils during testing. Polymer fibrillation could arise from surface imperfections or voids, acting as stress concentrations that subsequently expand under the action of the applied tensile stress to form the fibril structure [23, 24]. It was reported that the TB material has a random degree of porosity [2] which explains the development of polymer fibrils during mode I testing. Such behavior is known to be a major mechanism of increased fracture toughness [23, 24] and this is shown on
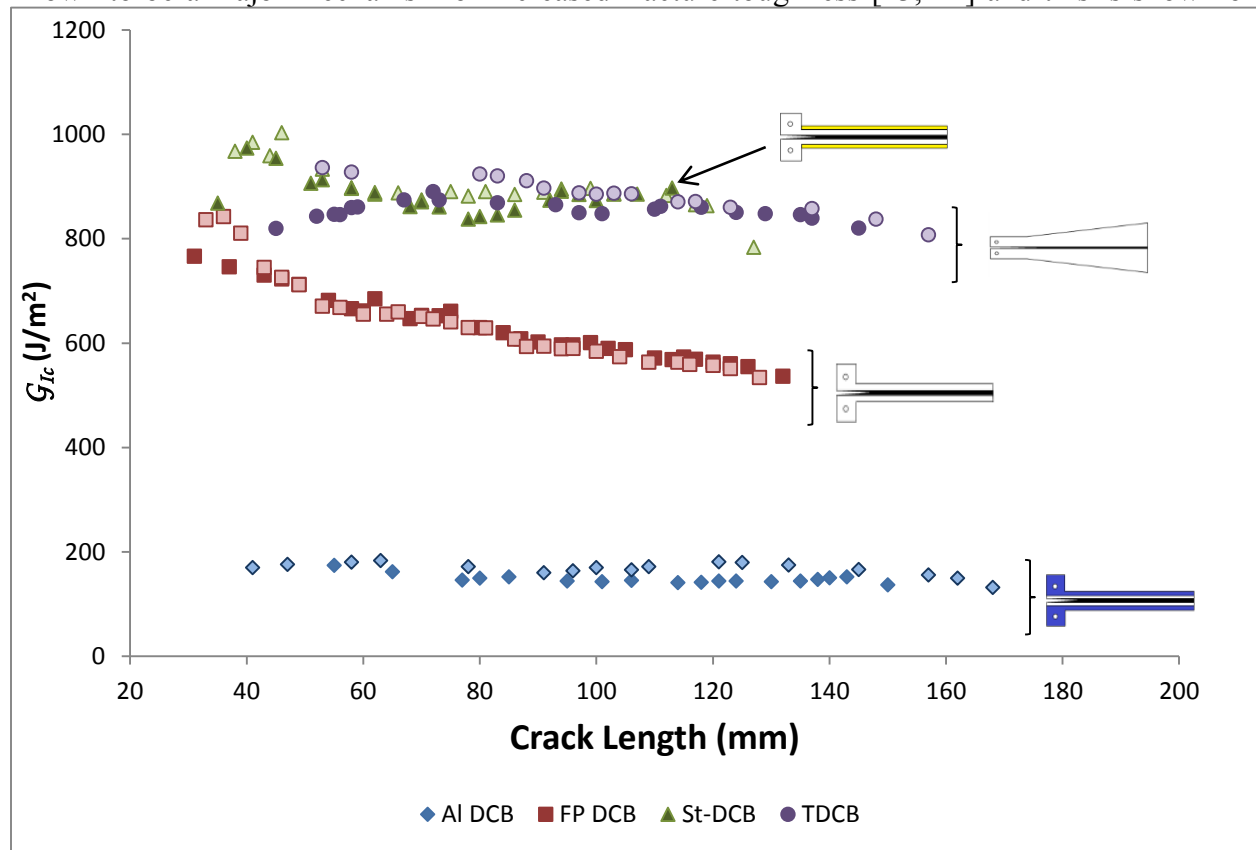
Figure 4 for all fully-printed specimens. SEM images also show signs of localized plasticity that may have been initiated at the boundaries of defects and voids produced by the printing process. It is believed that polymer blending occurs between the TB and VW, as the failure surface appears grey to the naked eye. This is expected as both VW and TB are deposited on each pass of the printer head, resulting in a potential interphase region that is much tougher than the less blended interface between the TB and VW.

The fully printed DCB resulted in higher values of G_{Ic}, but it is noted that the adherends experienced significant plastic deformation during testing, thereby dissipating energy and exaggerating the measured G_{Ic} values. While bonding steel plates to the adherends was thought to

reduce plastic deformation and dissipation, adding them made little difference. In fact, the steel plate-backed DCB configuration resulted in even larger G_{Ic} values compared to the non-reinforced, fully-printed configuration. This may be due to the larger amount of energy being dissipated to deform both the VW and the steel plating during testing. The fully printed TDCB also demonstrated similar trends of exaggerated fracture energies as with the DCBs, though this was not forseen as the tapered height was design to reduce adherend dissipation. It is noted that fabricating the TDCB required the most amount of polymer to print due to the tapered profile of the beam height, leading to much longer print times than the both the 3DP sandwich and DCBs.

3.2. Print Orientation

To evaluate the effects of print orientation, FP-DCB specimens were printed in three orientations ($\bar{x}yz$, $\bar{x}zy$, $\bar{y}xz$), as shown in the middle image of Figure 2. The variation of fracture energy against crack length for non-backed, fully-printed DCB specimens from the three print orientations is shown in Figure 6. It is noted that extensive polymer fibrillation occurs for all of the printed DCBs. Specimens printed in the $\bar{x}zy$ orientation, where the applied load during testing is perpendicular to the direction of the print build, are shown to have higher fracture toughness than the other two orientations, where the applied load is in the same direction of the print build. This corresponds with prior research that indicates that the strength of PolyJet materials is poor when the load is applied in the direction of the print build, wherein failure occurs predominantly at the interlayer boundaries [25, 26].
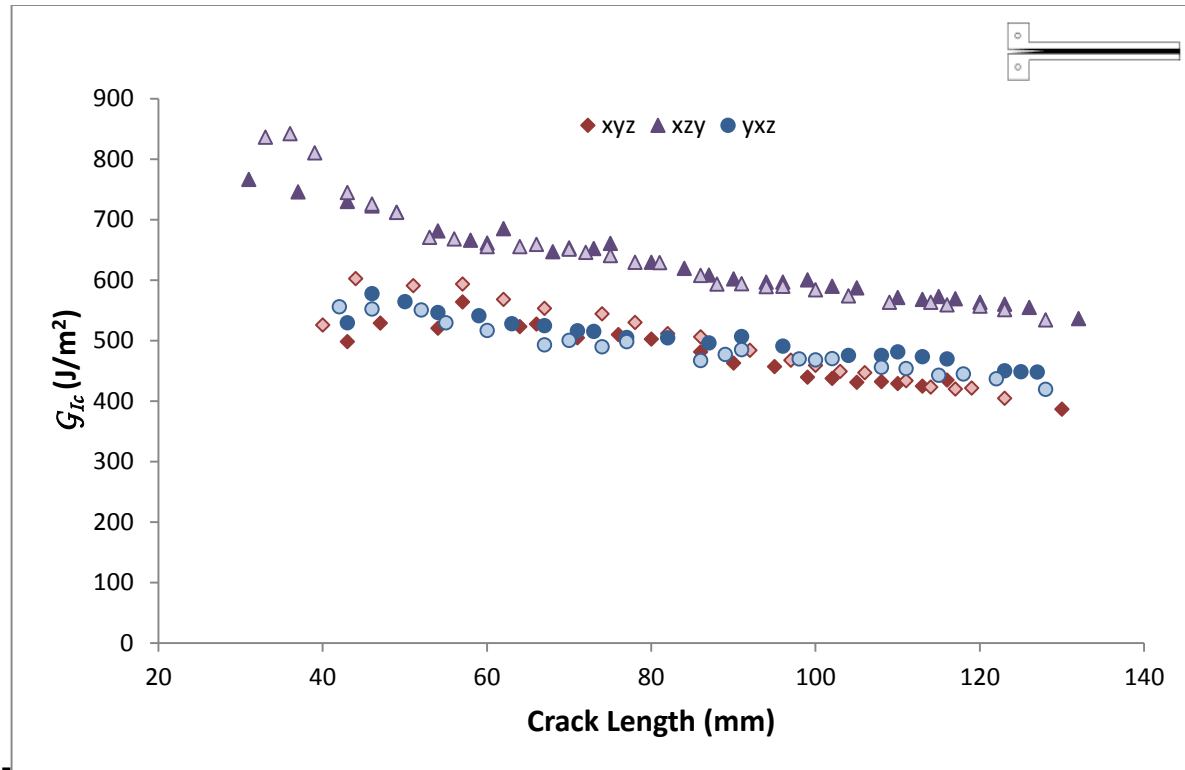
Figure 6. $\mathcal{G}_{Ic}$ vs. crack length for the fully-printed DCB configurations based on orientation

Figure 7b indicates that the failure surface of the $\bar{x}zy$ oriented specimen has a grey color or appearance that is evidence of polymer blending between TB and VW, possibly resulting in an interphase region that is much tougher than the less blended interface. For the specimens built in the $\bar{x}yz$ and $\bar{y}xz$ orientation, there is a clear distinction between the TB and VW sides of the fracture surface, suggesting a much lower degree of polymer blending as VW and TB were printed on separate passes of the print head. Thus, a TB (VW) layer would have deposited on a cured VW (TB) layer deposited in a previous pass. The SEM images indicated in Figure 7a and Figure 7c demonstrate a discretized failure surface as patches of TB, possibly polymer tufts, are randomly distributed across the failure surface. Such observations of discrete failures are reminiscent of spiral cracking as seen from the work of Dillard et al [27]. While such discrete failures from their work were seen to initiate from solvent exposure, it is predicted that the voids and defects produced by the printing process may have already weaken the TB enough to experience such failures. The FP DCBs were shown to experience significant plastic deformation during testing, which may have exaggerated the measured fracture energies shown above.
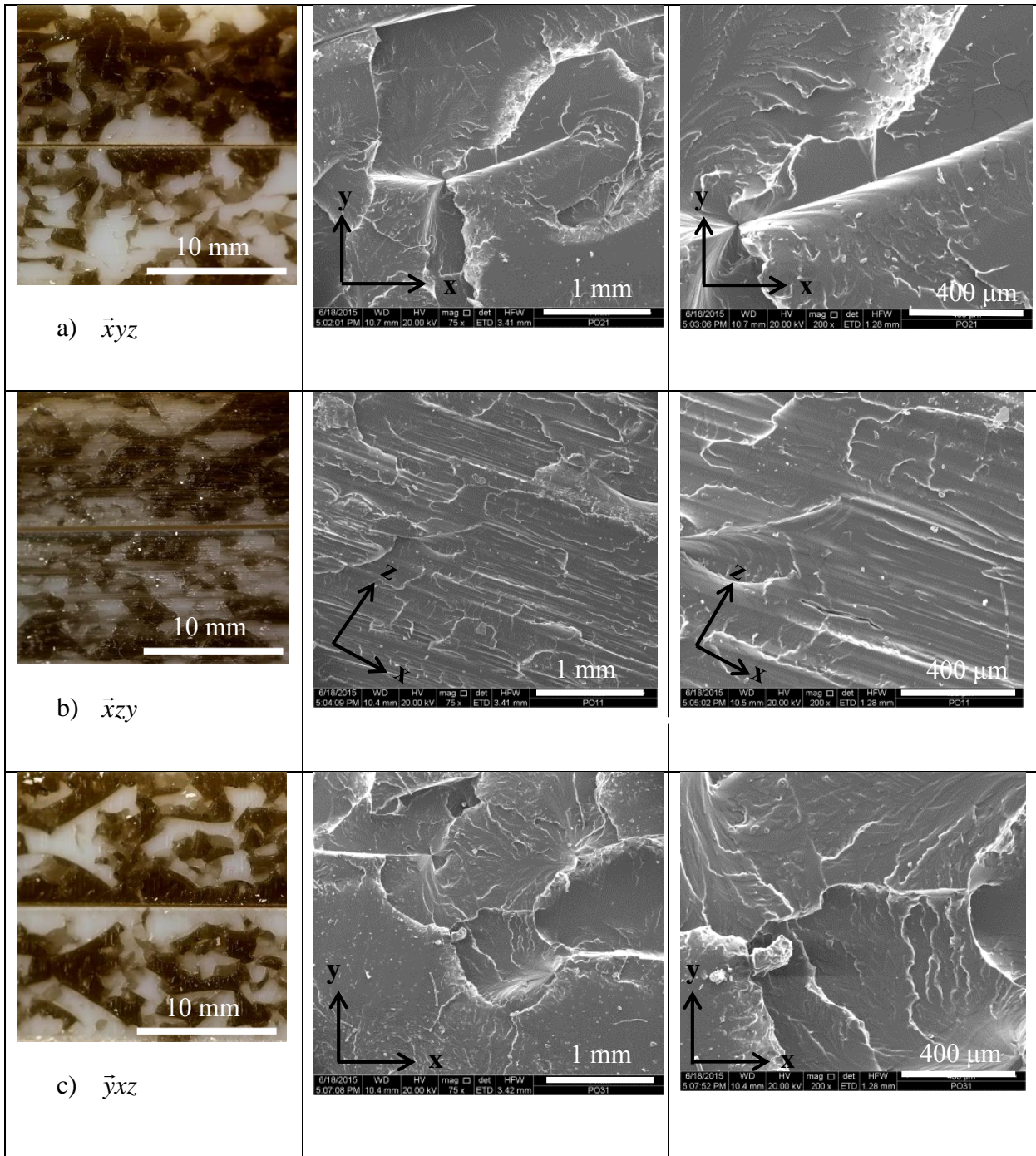
Figure 7. Failure surfaces and SEM images of fully printed DCBs printed in the a) $\vec{x}yz$, b) $\vec{x}zy$, and c) $\vec{y}xz$ orientation.

The Al-DCB strip is also printed in the same three orientations, as shown in the right image of Figure 2. The variation of fracture energy against crack length is shown on Figure 8. It is noted that there are significant differences in the measured fracture energies between the

aluminum and fully printed configurations. While the fracture energy of the fully printed DCB is seen to be higher in the $\bar{x}zy$ orientation, this is not seen for the aluminum configuration.
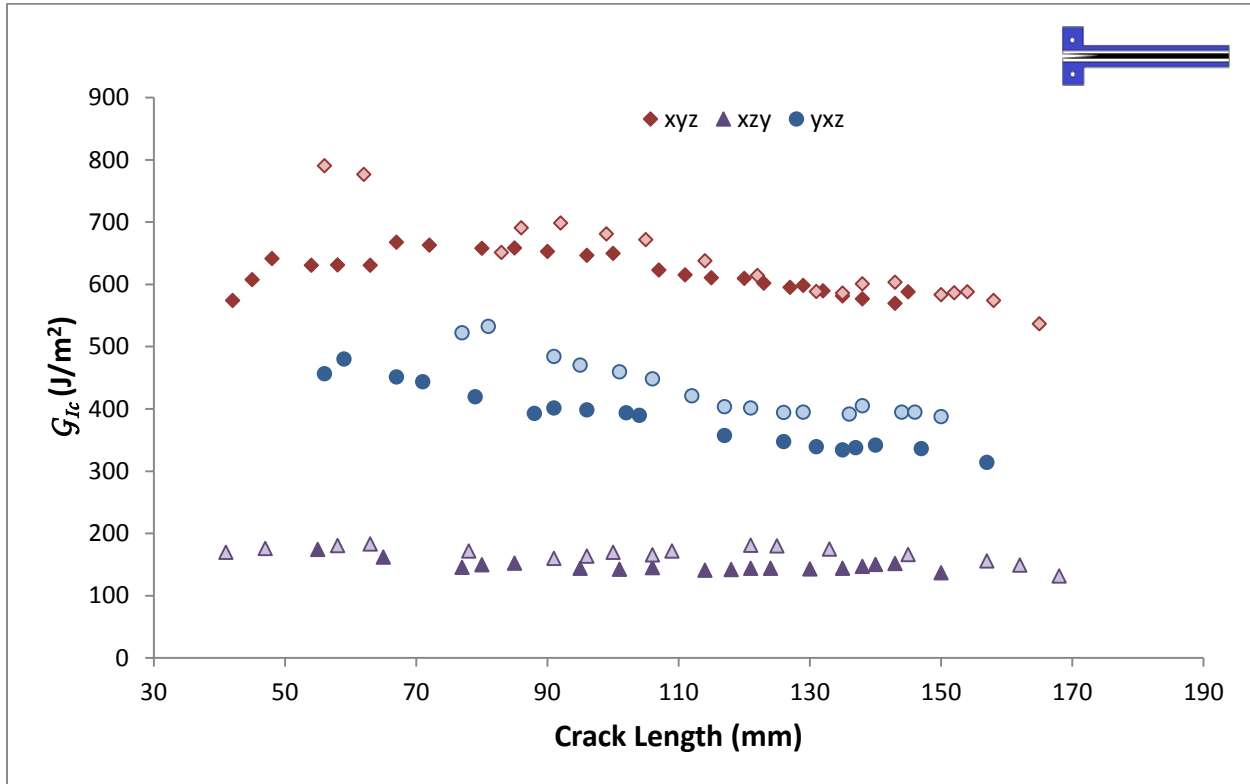
Figure 8. G_{Ic} vs. crack length for the Al-DCB configurations based on orientation.

As mentioned earlier, the failure of the Al-DCB printed in the $\bar{x}zy$ orientation appears largely interfacial and lacks the development of fibril structures that occurs for the other two orientations. This may be due to printing errors associated with printing specimens of a smaller length scale in contrast to the fully printed DCBs. The failure of Al DCB specimens for the $\bar{x}yz$ and $\bar{y}xz$ orientations are shown to alternate from one adherend interface to another, somewhat reminiscent of alternating locus of failures reported for adhesive joints [28-31]. Distinct polymer tufts are left on the failure surface after testing as shown on the top and bottom portions of Figure 7. Failure surfaces and SEM images of fully printed DCBs printed in the a) $\bar{x}yz$, b) $\bar{x}zy$, and c) $\bar{y}xz$ orientation. and Figure 9. While the FP-DCB showed that both the $\bar{x}yz$ and $\bar{y}xz$ directions were equivalent in fracture toughness, this is not seen in the Al-DCB configuration as the $\bar{x}yz$ orientation is shown to be the highest in terms of fracture toughness between the other orientations.
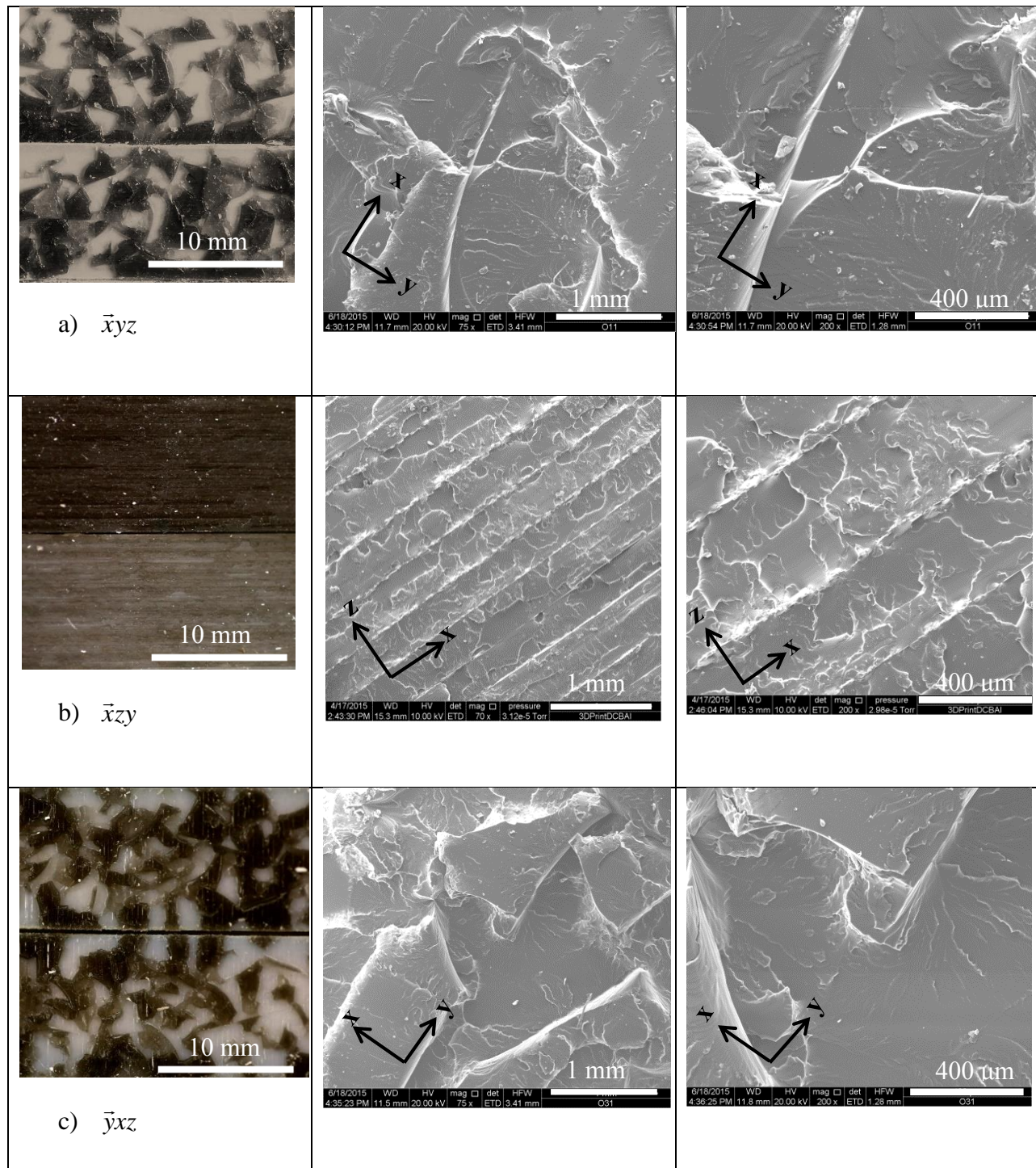
Figure 9. Failure surfaces and SEM images of Al-DCBs printed in the a) $\vec{x}yz$, b) $\vec{x}zy$, and c) $\vec{y}xz$ orientation.

3.3. Rate Dependency

To evaluate the rate dependency of the TB/VW interface, additional mode I tests were performed on the Al-DCB configuration at crosshead displacement rates of 0.01, 0.1 and 1 mm/min using the Al-DCB printed in the $\vec{x}yz$ orientation. The results are shown in Figure 10.

a)
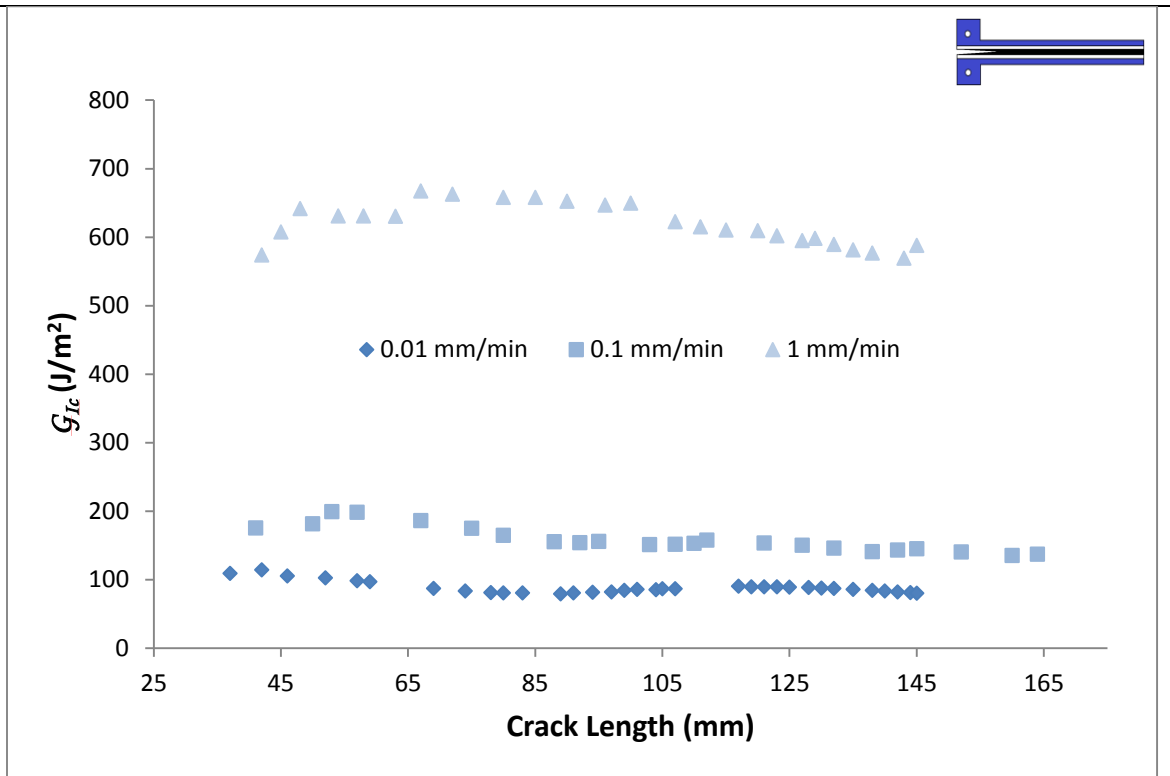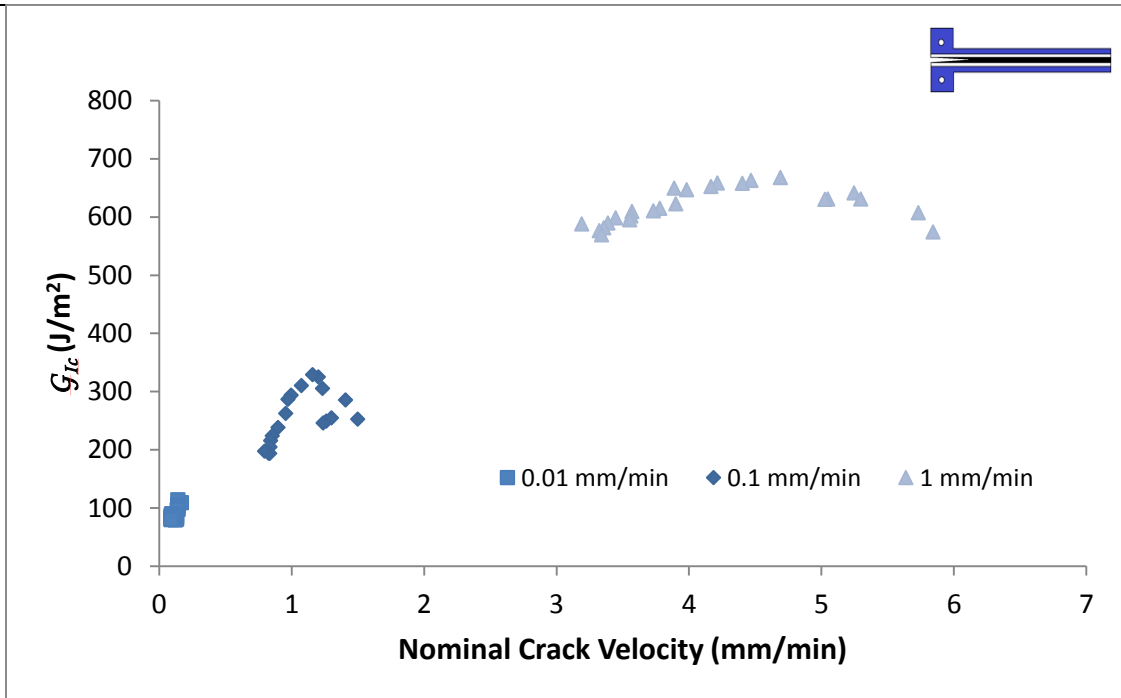
Figure 10. Fracture results for 3DP sandwich printed in the $\vec{x}yz$ orientation and tested at three crosshead displacement rates: a) $\mathcal{G}_{Ic}$ vs. crack length and b) $\mathcal{G}_{Ic}$ vs. crack velocity showing clear crack velocity dependence.

It is clearly shown that the fracture energy of the TB/VW interface is highly rate dependent, as the fracture energy is seen to increase with increasing displacement rate. The resulting failure surfaces are also dependent on displacement rate and are shown on Figure 11.

c)
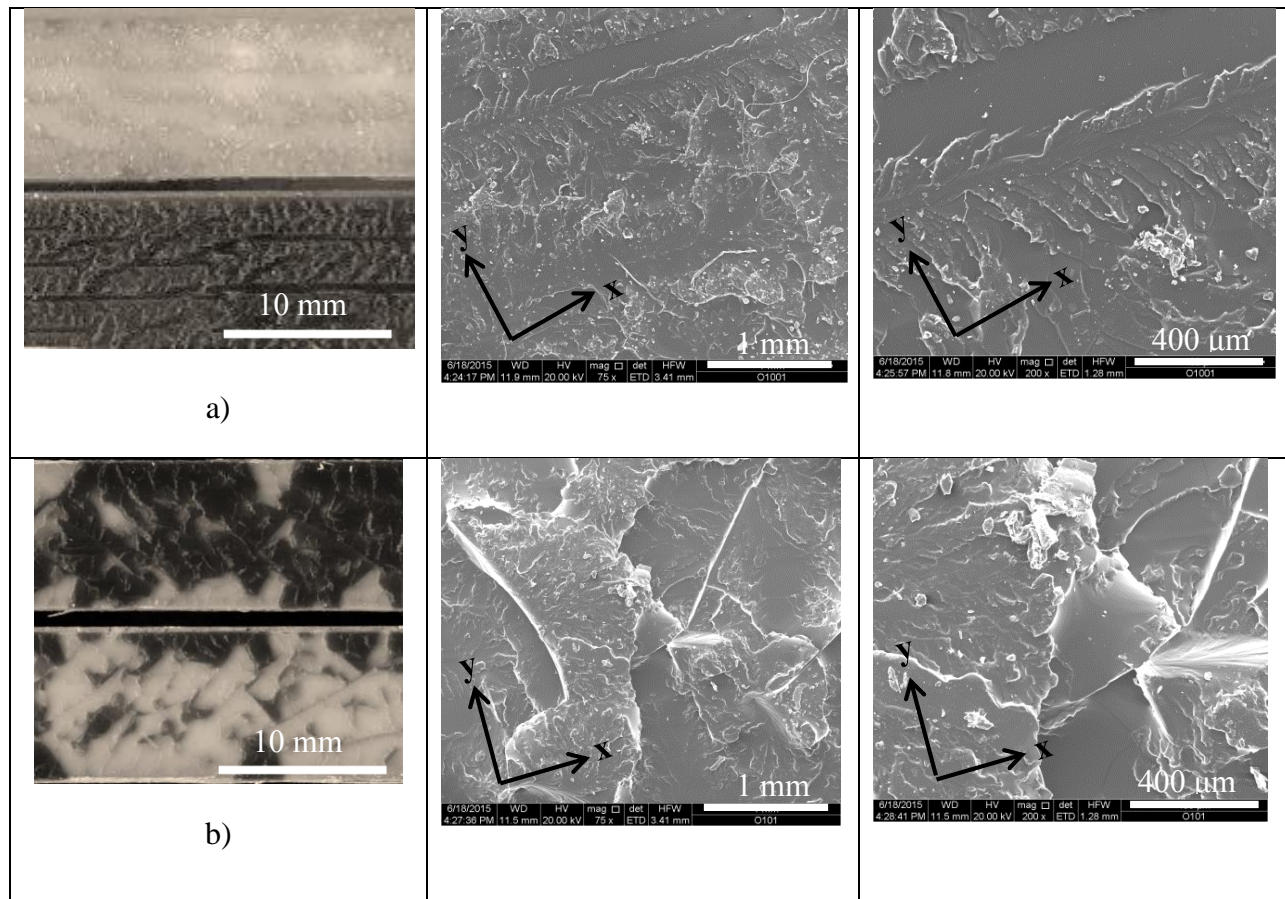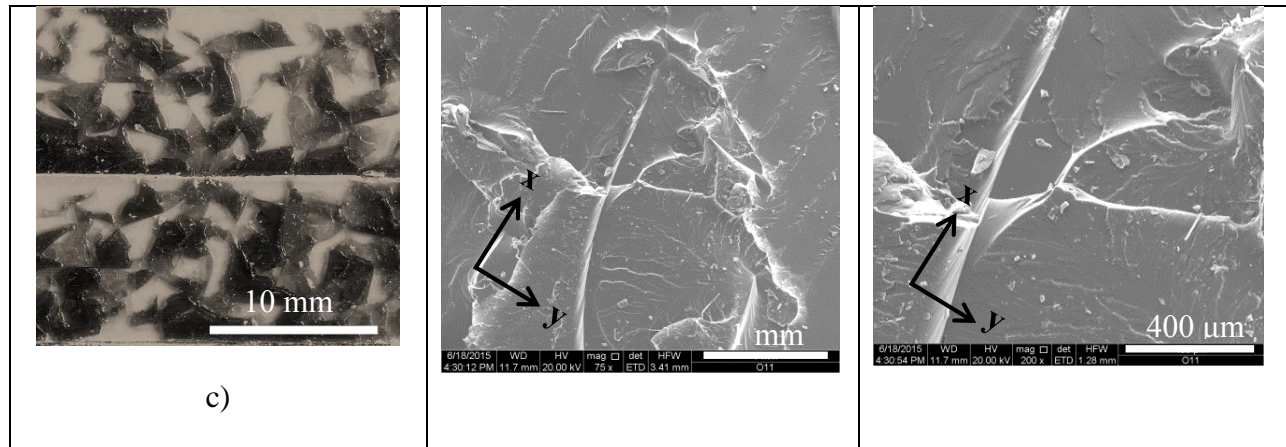
Figure 11. Failure surfaces and SEM images of Al DCB printed in the $\bar{x}yz$ orientation and tested at the displacement rate of a) 0.01 mm/min, b) 0.1 mm/min, and c) 1 mm/min

For the lowest displacement rate of 0.01 mm/min, the failure surface appears largely interfacial to the naked eye. As the displacement rate increases, the failure of the TB/VW interface becomes more cohesive, as the TB is being more evenly distributed across each adherend surface. Such differences to crack propagation and crack path selection was seen in the work of Chen et al., where they observed the effects of T stress for symmetric DCBs tested in both quasi-static and low-speed impact conditions [30]. They demonstrated that DCBs with positive T stress levels had a locus of failure that was dependent on the rate of crack propagation, where interfacial failures were seen under quasi-static rates and cohesive failures were seen for the low impact rates [30]. This was consistent with the earlier findings of Fleck et al., who demonstrated that adhesive layers with a positive T stress displayed a cohesive fracture trajectory [32]. In regards to the current findings above, it is speculated that the Al-DCB specimen may also have a positive level of T stress due to thermal and cure shrinkage of the materials [32]. Hence, similar results to Chen et al. [30] are observed when testing the materials at different displacements rates, though further evidence is needed to substantiate this claim.

3.4. Pattern Architecture

In addition to the original TB/VW interface, a gradient interface was printed wherein the central layers transition from VW to TB in the center, and back to VW. Note that in this configuration, VeroGrey60 (VG60), a mixture of TB with a majority of VW, is also incorporated in addition to TangoBlack60, which is a mixture of VW with a majority of TB. The test strips were printed in the $\bar{x}yz$ orientation. The results of the T-peel tests are shown below.
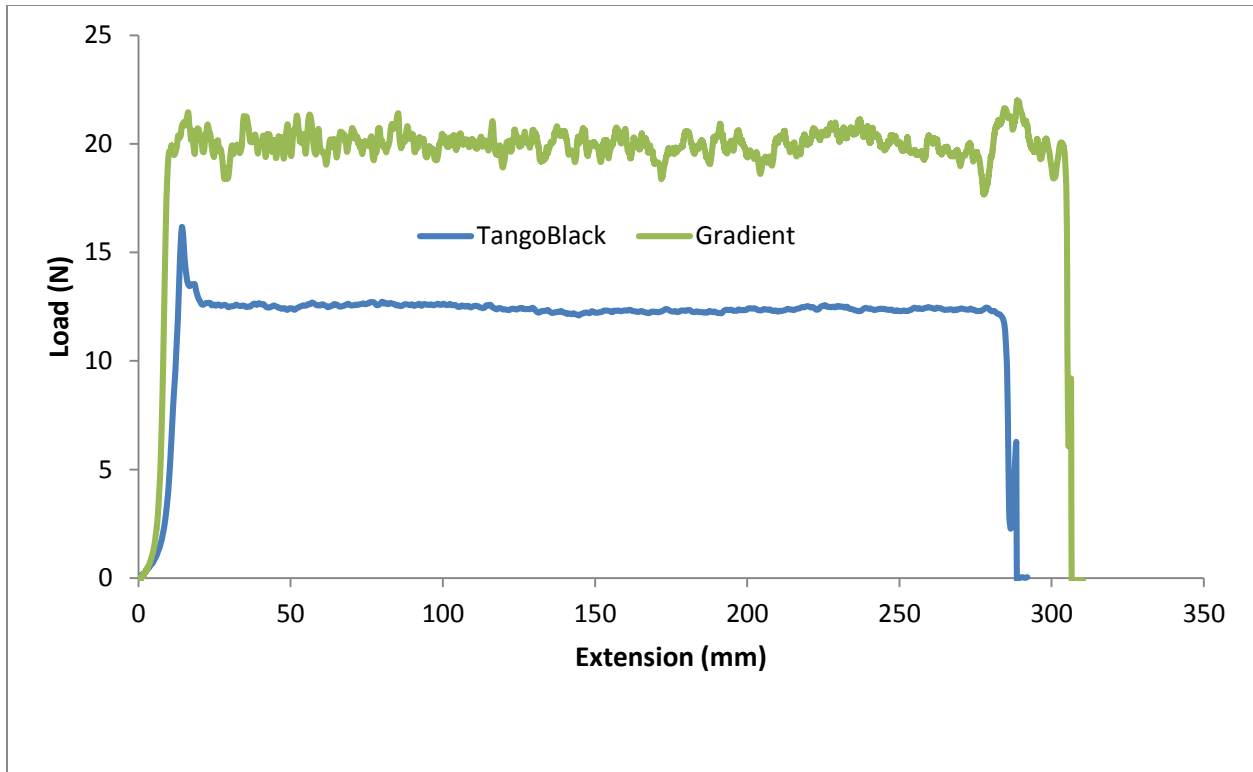
Figure 12. Load vs. extension curves from T-peel tests

	TB/VW	**Gradient**
Average Force (N)	12.40	20.08
Energy Release Rate (J/m^2)	2505	4057

Table 2. T-peel results

It is shown that the pure TB/VW configuration is the weakest in terms of peel. The failure surface shows a pure interfacial failure at the TB/VW interface. While the exact location of failure is not visually clear, the gradient transition had much better peel performance as it shows a 62% increase in average force and energy release rate when compared to pure TB/VW interface.
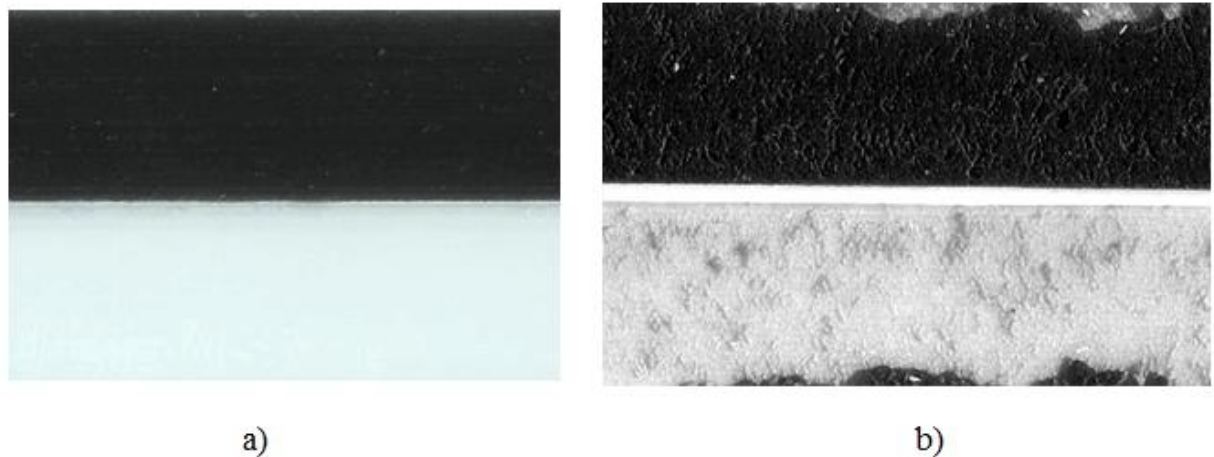
Figure 13. Failure surface of T-peel specimens. a) TB/VW and b) gradient

The failure surface for the gradient specimen is largely interfacial, where little material is left on one of the adherends. It is clearly seen that an improvement on peel performance can be accomplished by utilizing different print patterns and geometries at the central layers.

4. CONCLUSIONS

This study proposes several test configurations to assess the mode I fracture toughness of polyjet materials. Various DCB and TDCB configurations are constructed and tested to establish which specimen configuration would best represent the fracture toughness. It is demonstrated that all fully printed specimens experience some degree of polymer fibrillation and adherend plasticity during testing, which may have exaggerated the measured fracture energies. The addition of bonded steel plates on the adherend arms were not sufficient to reduce the plasticity effect. The fully printed TDCB demonstrated the same trends of exaggerated fracture energies for unknown reasons, as the tapered profile of the beam height was thought to limit adherend dissipation. It is noted that using the TDCB specimen requires using more VW material to print the tapered profile, leading to longer print times when compared to the other configurations. The 3DP sandwich bonded to Al adherends is thought to be most representative specimen for mode I testing of the polyjet materials as the Al adherends were able to minimize plastic dissipation of the adherends, though it required the longest time to fabricate. It is seen that 3DP sandwich specimens built in the $\bar{x}zy$ orientation has the lowest fracture toughness, though the reasons behind this are unclear. Given the small dimensional scale of the printed assembly, it is speculated that the roller introduced deformations and smearing of the materials that compromised the structural integrity of the printed assembly. Some blending between the support material and VW may have also occurred and led to the reduced properties and aforementioned failures seen above. It is predicted that increasing the VW boundary would reduce the likelihood of polymer blending from occurring between the two materials or other anomalous effects that would led to the very low fracture resistance of the Al-DCB specimens printed in this orientation. The failure surface of the TB/VW interface demonstrates a random fracture trajectory as TB is randomly dispersed and distributed between the adherend interfaces. SEM images for specimens printed in the $\bar{x}yz$ and $\bar{y}xz$ orientations indicate an alternating fracture surface that is somewhat reminiscent of alternating failures observe for adhesive joints

979

[28-31]. After subsequent development of fibrils during testing, polymer tufts of TB are left behind on the failure surface. Signs of localized plasticity are also observed around the polymer tufts, believing to have occurred at the boundary of defects or voids produced by the printing process.

The fracture energy is seen to be highly rate dependent, as an increase in displacement rate leads to increased fracture energies. Increasing the displacement rate also leads to failures that transition from purely interfacial to alternating cohesive failures. It is speculated that T stresses may have developed as a result of thermal and cure shrinkage printing. Such rate dependent failures are consistent with previous findings by Chen et al and Fleck et al. [30, 32], though more evidence is needed to substantiate this claim.

T-peel tests were performed on the Al-DCB specimens with different pattern architectures implemented at the central layers in order to observe any increased peel performance when compared to the TB/VW interface. It is demonstrated that the gradient pattern had much better peel performance than the TB/VW interface, being 62% higher in terms of both average peel force and energy release rate.

While the viscoelastic nature of polyjet materials tend to introduce complexities during deformation, it is shown that these materials can offer adequate fracture performance if the proper print parameters are selected. Other combinations of material and pattern architecture not considered in this study may offer other design options for enhanced fracture toughness.

5. ACKNOWLEDGMENTS

6. REFERENCES

1.   Kęsy, A. and J. Kotliński, *Mechanical properties of parts produced by using polymer jetting technology.* Archives of civil and mechanical engineering, 2010. **10**(3): p. 37-50.
2.   Moore, J.P. and C.B. Williams. *Fatigue Characterization of 3D Printed Elastomer Material.* in *International Solid Freeform Fabrication Symposium.* 2012.
3.   Berman, B., *3-D printing: The new industrial revolution.* Business horizons, 2012. **55**(2): p. 155-162.
4.   Upcraft, S. and R. Fletcher, *The rapid prototyping technologies.* Assembly Automation, 2003. **23**(4): p. 318-330.
5.   Ahn, S.-H., et al., *Anisotropic material properties of fused deposition modeling ABS.* Rapid Prototyping Journal, 2002. **8**(4): p. 248-257.
6.   Perez, A.R.T., D.A. Roberson, and R.B. Wicker, *Fracture surface analysis of 3D-printed tensile specimens of novel ABS-based materials.* Journal of Failure Analysis and Prevention, 2014. **14**(3): p. 343-353.

7.   Bellini, A. and S. Güçeri, *Mechanical characterization of parts fabricated using fused deposition modeling.* Rapid Prototyping Journal, 2003. **9**(4): p. 252-264.

8.   Barclift, M.W. and C.B. Williams. *Examining variability in the mechanical properties of parts manufactured via polyjet direct 3D printing*. in *International Solid Freeform Fabrication Symposium, August*. 2012.

9.   ASTM D638-14, Standard Test Method for Tensile Properties of Plastics, ASTM International, West Conshohocken, PA, 2014.

10.   ASTM D3039 / D3039M-14, Standard Test Method for Tensile Properties of Polymer Matrix Composite Materials, ASTM International, West Conshohocken, PA, 2014.

11.   *Plastics - determination of tensile properties - part 1*, in *ISO 527-1*. International Standards Organization.

12.   *Plastics - determination of tensile properties - part 2*, in *ISO 527-2*. International Standards Organization.

13.   Sugavaneswaran, M. and G. Arumaikkannu, *Modelling for randomly oriented multi material additive manufacturing component and its fabrication.* Materials & Design, 2014. **54**: p. 779-785.

14.   *VeroWhitePlus PolyJet Materials Details | RedEye 3D Printing Services*. 2015; Available from: http://www.redeyeondemand.com/verowhite-polyjet/.

15.   *Tango Materials | 3D Modeling 3D Printing Materials, Rubber-Like*. 2015; Available from: http://www.3dprinterscanada.com/tango-materials.php.

16.   *Determination of the mode I adhesive fracture energy, GIC, of structural adhesives using the double cantilever beam (DCB) and tapered double cantilever beam (TDCB) specimens*, in *BS 7991:2001*. 2001.

17.   ASTM-D3433-99, *Standard Test Method for Fracture Strength in Cleavage of Adhesives in Bonded Metal Joints*, in *Annual Book of ASTM Standards*. 2001, ASTM: West Conshohocken. p. 225-231.

18.   ASTM-D1876, *Peel Resistance for Adhesives, T-Peel Test* American Society for Testing and Materials: West Conshohocken, PA.

19.   Blackman, B.R.K., et al., *Measuring the mode I adhesive fracture energy, GIC, of structural adhesive joints: the results of an international round-robin.* International Journal of Adhesion and Adhesives, 2003. **23**(4): p. 293-305.

20.   Karac, A., et al., *Modelling the fracture behaviour of adhesively-bonded joints as a function of test rate.* Engineering Fracture Mechanics, 2011. **78**(6): p. 973-989.

21.   Blackman, B., et al., *The calculation of adhesive fracture energies in mode I: revisiting the tapered double cantilever beam (TDCB) test.* Engineering Fracture Mechanics, 2003. **70**(2): p. 233-248.

22.   ASTM ISO / ASTM52921-13, Standard Terminology for Additive Manufacturing-Coordinate Systems and Test Methodologies, ASTM International, West Conshohocken, PA, 2013.

23.   Kinloch, A.J. and R.J. Young, *Fracture behaviour of polymers*. 1983: North-Holland.

24.   Argon, A.S., *The physics of deformation and fracture of polymers*. 2013: Cambridge University Press.

25.   Cazón, A., P. Morer, and L. Matey, *PolyJet technology for product prototyping: Tensile strength and surface roughness properties.* Proceedings of the Institution of Mechanical Engineers, Part B: Journal of Engineering Manufacture, 2014. **228**(12): p. 1664-1675.

26. Kim, G. and Y. Oh, *A benchmark study on rapid prototyping processes and machines: quantitative comparisons of mechanical properties, accuracy, roughness, speed, and material cost.* Proceedings of the Institution of Mechanical Engineers, Part B: Journal of Engineering Manufacture, 2008. **222**(2): p. 201-215.

27. Dillard, D.A., et al., *Spiral Tunneling Cracks Induced by Environmental Stress Cracking in LaRC™-TPI Adhesives.* The Journal of Adhesion, 1994. **44**(1-2): p. 51-67.

28. Chen, B. and D.A. Dillard, *The effect of the T-stress on crack path selection in adhesively bonded joints.* International journal of adhesion and adhesives, 2001. **21**(5): p. 357-368.

29. Chen, B. and D.A. Dillard, *Numerical analysis of directionally unstable crack propagation in adhesively bonded joints.* International journal of solids and structures, 2001. **38**(38): p. 6907-6924.

30. Chen, B., et al., *Crack path selection in adhesively bonded joints: the roles of external loads and speciment geometry.* International journal of fracture, 2002. **114**(2): p. 167-190.

31. Chai, H., *A note on crack trajectory in an elastic strip bounded by rigid substrates.* International journal of fracture, 1986. **32**(3): p. 211-213.

32. Fleck, N.A., J.W. Hutchinson, and S. Zhigang, *Crack path selection in a brittle adhesive layer.* International Journal of Solids and Structures, 1991. **27**(13): p. 1683-1703.